THE JOURNAL OF PHYSICAL CHEMISTRY LETTERS
A JOURNAL OF THE AMERICAN CHEMICAL SOCIETY

pubs.acs.org/JPCL Letter

Dirac Fermions and Flat Bands in Phosphorus Carbide Nanotubes: Structural and Quantum Phase Transitions in a Quasi-One-Dimensional Material

Shivam Sharma, Chenhaoyue Wang, Hsuan Ming Yu, and Amartya S. Banerjee*

Cite This: https://doi.org/10.1021/acs.jpclett.6c00091 Read Online

ACCESS | Metrics & More | Article Recommendations | Supporting Information

ABSTRACT: Chemically realistic quasi-one-dimensional (1D) materials in which Dirac Fermions and highly degenerate flat bands coexist intrinsically at the Fermi level are exceedingly rare, while representing a highly desirable platform for correlated and topological quantum phenomena. Here, using specialized symmetry-adapted first-principles calculations we predict a new class of nanomaterials—phosphorus carbide nanotubes (P_2C_3NTs)—obtained by rolling monolayer P_2C_3, a two-dimensional material shown in a previous letter to host "double Kagome bands". Both armchair and zigzag P_2C_3NTs are stable at room temperature and feature the rare coexistence of Dirac crossings and multiple flat bands at the Fermi level inherited from the underlying honeycomb−Kagome lattice, with the flat bands resilient to elastic deformations. Under large strain, the structure transforms from honeycomb−Kagome to "brick-wall", accompanied by multiple coupled structural and quantum phase transitions. We also uncover localized edge states, spin splitting from vacancies and dopants, and strain-tunable magnetism. Together, these results establish P_2C_3NTs as a chemically specific and mechanically tunable 1D material platform with potential applications in quantum hardware and spintronics.

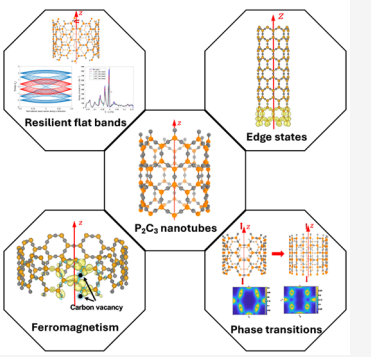

A significant amount of contemporary materials research is directed toward the discovery, synthesis, and characterization of nanomaterials and nanostructures featuring exotic electronic states. Such materials can manifest remarkable and unusual physical properties, leading to promising applications in quantum technologies, spintronic devices, and next-generation microelectronics.[1−9] Two well-known examples of such electronic states, contrasting conventional parabolic dispersion in common semiconductors, are ones exhibiting linear dispersion[10] (e.g., Dirac cones in graphene) and ones without dispersion (i.e., electronic *flat bands*, e.g. in Kagome lattices[11]). The former is associated with massless fermions with high carrier mobility, leading to unconventional electronic,[12] transport,[13] optical[14] and topological properties.[15,16] The latter is often associated with infinitely massive fermions with quenched kinetic energies and spatially localized electronic states that interact in the strongly correlated regime. Such interaction leads to fascinating electronic phases with collective properties,[17] e.g. superconductivity,[18−20] ferromagnetism,[21,22] Wigner crystallization,[23] and the fractional quantum Hall effect.[24,25]

Bulk and nanomaterials featuring the Kagome lattice host both these types of electronic states, thus driving a wide variety of interesting properties associated with these materials, and leading to a proliferation of studies on them in recent years.[26−32] Generally, the Dirac crossings and flat bands in Kagome materials do not appear simultaneously at the Fermi level[26−28,33−35]—instead, their electronic structure usually exhibits *quadratic band touching* points. However, from the perspective of applications, the simultaneous presence of Dirac cones and flat bands at the Fermi level can be particularly intriguing: Dirac cones contribute to the emergence of electronic edge states, while flat bands promote strongly correlated behavior, rendering the material multifunctional. Despite this promise, chemically realistic materials in which Dirac points and highly degenerate flat bands coexist intrinsically at the Fermi level remain exceedingly rare. In most known Dirac materials, such as graphene and carbon nanotubes, the electronic structure near the Fermi level is dominated by linearly dispersing bands with a vanishing density of states. Conversely, flat-band systems based on Kagome or related lattices typically exhibit quadratic band-touching points or flat bands that are energetically displaced from the Fermi level. As a result, achieving the coexistence of Dirac fermions and dispersionless electronic states at the Fermi level generally requires fine-tuning through external fields, chemical modification, or artificial lattice engineering.

Motivated by this challenge, a number of studies have explored the Honeycomb-Kagome (HK) and Lieb lattices,

Received: January 12, 2026
Revised: March 27, 2026
Accepted: March 31, 2026

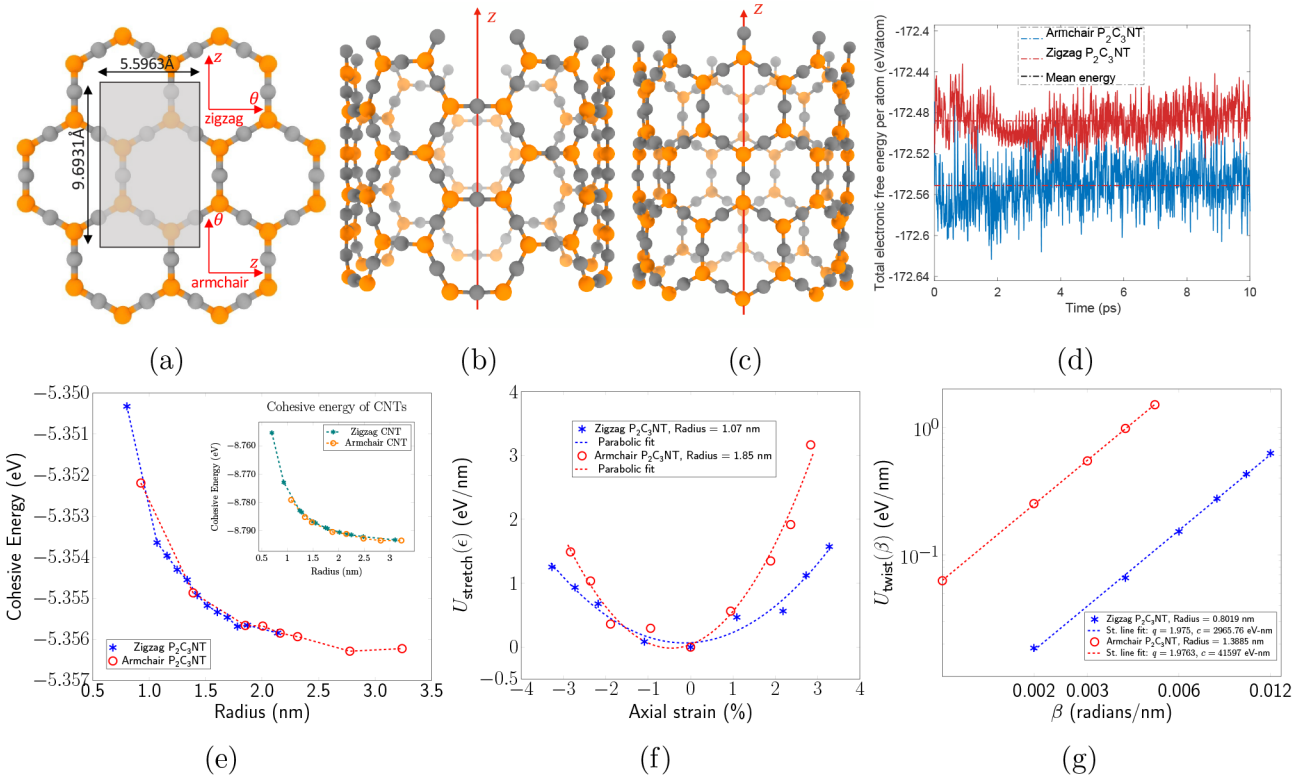

Figure 1. (a) Pristine 2D P_2C_3 lattice showing the roll-up direction, θ for the zigzag and armchair nanotubes and z is in the direction of nanotube's axis. Two types of P_2C_3NTs is investigated in this work: (b) Armchair (n, n) and (c) zigzag (n, 0) nanotubes, where, n is the cyclic group order about the tube axis. (d) System energy variation over ab initio molecular dynamics (AIMD) trajectories at temperatures 315 K for an (12,12) armchair (blue) and a (15,0) zigzag (red) P_2C_3NTs. Dashed line denotes the mean energy. (e) Cohesive energy of zigzag and armchair P_2C_3NTs. (f) Extensional energy per unit length as a function of axial strain for two representative P_2C_3NTs. Dotted curves indicate parabolic fits of the data to an ansatz of the form $U_{stretch}(\epsilon) = c \times \epsilon^2$. (g) Twist energy per unit length as a function of angle of twist per unit length for two representative nanotubes (both axes logarithmic). Dotted lines indicate straight line fits of the data to an ansatz of the form $U_{twist}(\beta) = c \times \beta^q$. The exponent q is nearly 2.0 in both cases, suggesting linear elastic behavior.

which do exhibit coexisting Dirac dispersions and flat bands, at least in idealized tight-binding models.[36,37] In particular, the HK lattice (also referred to as the Honeycomb Splitgraph[38]) can be envisioned as a combination of conventional honeycomb and Kagome lattices, and its electronic states can be deduced accordingly.[36,38,39] While realizations of the Lieb lattice in realistic 2D materials remain scarce, a number of recent contributions have computationally explored planar materials of the type A_2B_3, that structurally feature the HK lattice. Most thermodynamically stable materials proposed in this category constitute metal oxides[40−43] or carbides,[44−47] with some of these materials having been associated with fascinating properties such as non-trivial topological phases and half metallicity. Although these materials exhibit Dirac cones near the Fermi level, they either lack a flat band at the Fermi level or exhibit one that is misplaced. Such deviations arise because the specific chemical characteristics of the atoms involved — including, orbital hybridization states and different on-site energies — can cause differences in the electronic structure from idealized tight-binding models of HK lattices.

A notable exception to these limitations was reported in a previous letter to this journal by Huang et al.,[48] who introduced a new form of phosphorus carbide (P_2C_3) featuring so-called "double Kagome bands". In this two-dimensional material with HK geometry, the out-of-plane p_z orbitals of both phosphorus and carbon atoms combine to produce the rare coexistence of Dirac Fermions and strongly correlated dispersionless electronic states directly at the Fermi level. In this letter, we extend this work by studying P_2C_3 nanotubes (P_2C_3NTs), thereby exploring a far less studied class of nanomaterials (i.e., quasi-one-dimensional or 1D nanostructures) with fascinating properties. From the perspective of quantum materials design, the realization of such Dirac−flat-band coexistence in a quasi-one-dimensional geometry is particularly appealing, as reduced dimensionality enhances electronic interactions and enables strong coupling between mechanical deformation, electronic structure, and emergent quantum phases. Our findings unveil a range of noteworthy electronic, structural, and magnetic characteristics unique to these nanotubes. While P_2C_3 nanotubes are yet to be synthesized, we anticipate that our computational and theoretical investigations will provide impetus for future experimental efforts.[49,50] Indeed, both phosphorus and carbon are already well-known for their ability to form a large number of elemental allotropes, and a number of varieties of stable monolayer phosphorus carbide have also been investigated in recent years.[51−54] Relatedly, some studies have suggested the possibility of creating quasi-one-dimensional forms of such compounds.[55−57] These previous findings not only highlight the growing interest in low-dimensional materials with unique properties, but also lend support to the experimental synthesizability of P_2C_3NTs in the near future, thereby bolstering the relevance of the current work (also see the Supporting Information (SI)).

https://doi.org/10.1021/acs.jpclett.6c00091
J. Phys. Chem. Lett. XXXX, XXX, XXX−XXX

We arrive at P_2C_3NTs through a "roll-up" operation,[58] in which structurally relaxed planar P_2C_3[48] (with hexagonal lattice parameters $a = b = 0.569$ nm) is folded into seamless cylinders. The hexagonal unit cell in the planar structure comprises two phosphorus and three carbon atoms that are strategically positioned at the corners of the hexagonal lattice and the center of the edges of the hexagons, respectively (see Figure 1). This ensures that the p_z orbitals of P and C atoms are oriented radially outward in the resulting nanotubes and can overlap to feature HK-like electronic bands in a quasi-one-dimensional setting. Further details of the orbital origin of these bands in P_2C_3NTs are described below and in the Supporting Information (SI). The resulting nanotubes are classified by nonnegative integers (n, m), i.e., the chirality indices of the tube, which specify the direction of rolling. Here, we have exclusively studied armchair (n, n) and zigzag $(n, 0)$ tubes (see Figure 1b and 1c), in their pristine and distorted states. Our computational studies are enabled by a recently developed suite of real-space first-principles simulation techniques, that take advantage of the cyclic and helical symmetries inherent to 1D nanostructures.[59−64] Exploitation of global symmetries allows this framework to efficiently simulate pristine or deformed nanotubes (of any chirality) using Kohn−Sham Density Functional Theory (KS-DFT),[65,66] while considering only a few atoms in the computational unit cell. Our investigations of mechanical and electronic properties using these techniques generally used 5 or 10 representative atoms (i.e., just one or two formula units of P_2C_3) in the symmetry-adapted unit cells (Figure 1a). Typically, such simulations also employed a discretization of the reciprocal space associated with the helical symmetry, which we refer to as η-point sampling (in analogy to *k-point sampling* in solid state systems). Notably, many of such calculations would require an impractically large number of atoms in the computational unit cell if conventional first-principles methods (e.g., plane-wave-based approaches) were used.[59,61] Simulation cells containing more atoms were employed for ab initio molecular dynamics and magnetism calculations.

Additional symmetry-related parameters for the simulations are as follows. The screw-transformation (or helical symmetry operation) used to describe the nanotubes has an associated pitch of $\tau = 0.55963$ and 0.96931 nm, for undeformed armchair and zigzag nanotubes, respectively. Changes in τ allow examination of the effects of uniaxial extensions and compressions on the material. Concurrently, a scalar parameter $0 \leq \alpha < 1$ represents applied twist to the structure, with $\beta = 2\pi\alpha/\tau$ denoting the twist per unit length. The nanotubes are also associated with cyclic symmetry about the tube axis, with the rotation angle $\Theta = 2\pi/\mathcal{N}$ being directly related to the tube chirality indices (e.g., $n = \mathcal{N}$ for zigzag $(n, 0)$ and armchair (n, n) tubes).

For the majority of our computations, we employed Helical DFT, a finite difference based implementation of symmetry adapted Kohn−Sham density functional theory.[59,61,63] We used 12th order finite differences with a vacuum padding of 10 Bohr in the nanotube radial direction. The Perdew−Wang parametrization[67] of the local density approximation[66] was chosen as the exchange-correlation functional. Furthermore, norm conserving pseudopotentials,[68,69] and 1 mHa of smearing using the Fermi−Dirac distribution were chosen. Self-consistent field iteration convergence was achieved via the Periodic Pulay scheme.[70] To reduce computational burden, Helical DFT simulations were conducted in three successive phases, with increasing levels of discretization fineness[32] (see SI for further details). Additionally to augment Helical DFT results, the Quantum Espresso[71,72] and SPARC[64,73−75] codes were used for calculations involving projected density of states (pDOS), magnetism effects due to vacancies and dopants, 2D P_2C_3 sheets, and some ab initio molecular dynamics runs.

We used our simulations to analyze various structural properties of P_2C_3NTs and to assess their stability. The cohesive energy depicted in Figure 1e shows monotonically decreasing behavior from −5.350 eV to −5.457 eV as the radius of zigzag and armchair nanotubes is increased from 0.5 to 3.5 nm. This is consistent with the expectation that tubes of larger radius are energetically more favorable due to the reduced elastic bending energy of the 2D sheet. In contrast to these numbers, the corresponding cohesive energy value for a conventional phosphorene nanotube[76,77] of approximately 0.7 nm radius is about −4.22 eV, and it is about −8.77 eV for a conventional carbon nanotube[78] (CNT) of similar radius (Figure 1e inset). These intermediate cohesive energy values of P_2C_3NTs are strongly suggestive of their synthesizability. The bending modulus of the planar P_2C_3 sheet comes out to be 0.1404 and 0.1520 eV when the sheet is bent in the armchair and zigzag directions, respectively. These values indicate that the sheet bending modulus of P_2C_3 is approximately one-tenth of that observed for conventional graphene, estimated to be around 1.5 eV,[62] The phonon stability of P_2C_3 sheets has been investigated earlier[48] and no unstable modes were found. Based on band-folding considerations,[79−81] such calculations are also likely to be indicative of the stability of P_2C_3NTs at 0 K, especially given the low elastic energies associated with folding P_2C_3 sheets into tubes. To assess the stability of P_2C_3NTs at finite temperature, we performed AIMD calculation at room temperature for several nanotubes (both zigzag and armchair varieties). Supercells containing 60 or more atoms—i.e., several copies of the unit cell in the cyclic and axial directions—were employed, in order to capture potential long-wavelength instabilities. The tubes were observed to be stable throughout the simulation duration (up to 10 ps). The variation of the system's energy for two representative P_2C_3NTs is shown in Figure 1d.

The kinetic stability of the P_2C_3NTs investigated in this letter is a promising sign of their synthesizability. Earlier Huang et al.[48] have demonstrated a methodology to grow phosphorus carbide monolayer on silver (Ag) (111) substrate. They found that the lattice mismatch between P_2C_3 and Ag (111) substrate is less than 1.6% and the adhesion energy between them is −4.73 eV/atom. After synthesizing P_2C_3, the target etching of the silver layer can cause the 2D material to curl up and result in P_2C_3NTs[82] as illustrated in the Supporting Information (Figure S7). The lower bending stiffness of P_2C_3 sheets in comparison to graphene and phosphorene will likely make it easier for the material to fold up into nanotubes.

To investigate mechanical properties of P_2C_3NTs, particularly their response to torsional and uniaxial strain, we performed Helical DFT simulations with variations in the symmetry group parameters used to define the nanotube.[59] From these simulations, the energy per unit length of the deformed system, $U_{\text{deformed}}(x)$ may be calculated as a function of the strain parameter x, and the corresponding stiffness k may be obtained as $k = \left.\frac{\partial^2 U_{\text{deformed}}(x)}{\partial x^2}\right|_{x=0}$. Further details of

https://doi.org/10.1021/acs.jpclett.6c00091
J. Phys. Chem. Lett. XXXX, XXX, XXX−XXX

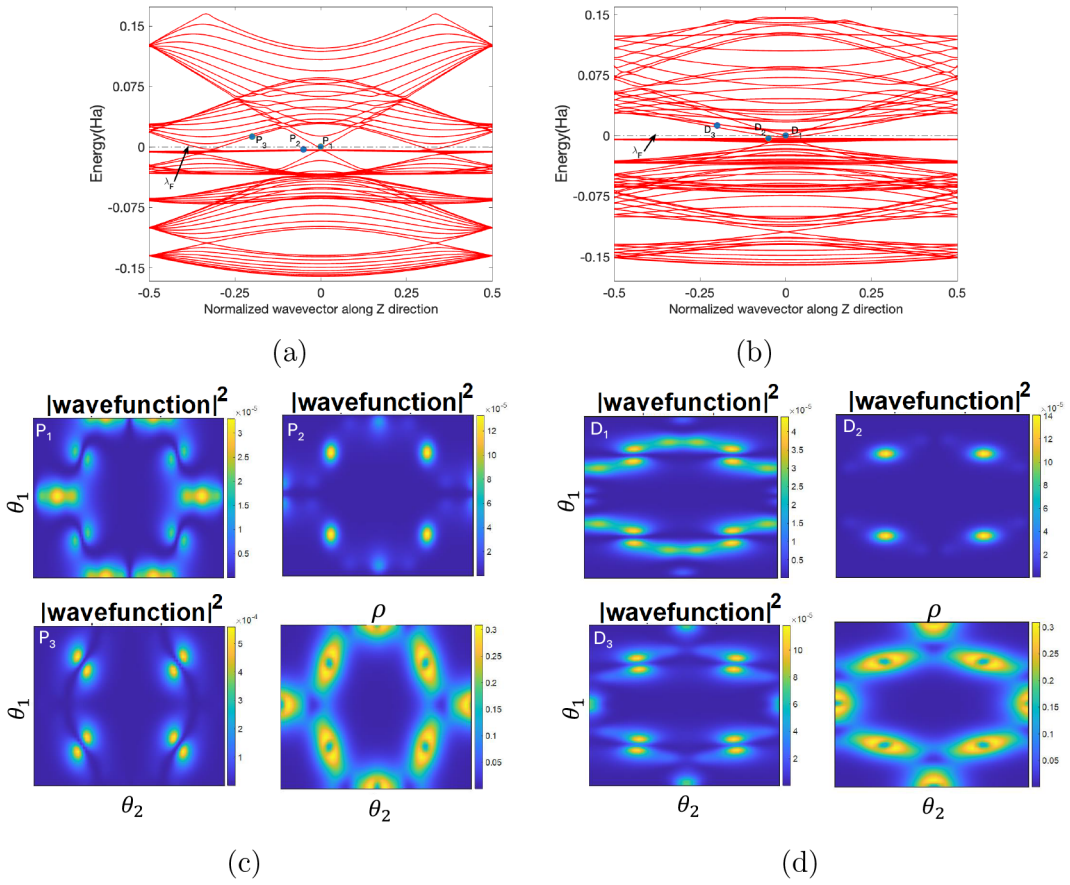

Figure 2. (a) and (b) show the band diagram of undeformed (9,9) armchair and (12,0) zigzag P_2C_3NTs, respectively. The Fermi level λ_F corresponds to the x-axis. (c) shows the electronic states (square of absolute value of wave function) associated with P_1, P_2 and P_3 points shown in (a). The bottom right panel is electron density. (d) shows the square of the wave function for the electronic states associated with the D_1, D_2 and D_3 points shown in (b). The bottom right panel is the electron density. A slice of electronic fields at an average radial distance of the atoms in the computational domain is shown in each case. θ_1, θ_2 denote helical coordinates that parametrize the tube surface at a fixed radial distance.

calculating $U_{\text{deformed}}(x)$ and the associated stiffness parameter, for torsional and uniaxial strains are provided in the SI. For torsional simulations, we imposed twists of up to about β = 4.5° per nanometer, the acknowledged limit of linear response for conventional CNTs.[58] Our investigation shows that the twisting deformation energy for P_2C_3NTs is very nearly quadratically dependent on the twist per unit length, i.e., these tubes also exhibit linear elastic behavior within this range (Figure 1g). In particular, we estimate from the data that the torsional stiffness constant (k_{twist}) for a zigzag P_2C_3NT of radius about 0.80 nm is 207.53 eV/nm, while it is 956.10 eV/nm for an armchair nanotube of radius about 1.4 nm. To compare these numbers with those of conventional CNTs, we note that CNTs are known to show behavior consistent with continuum theory,[58,61] wherein k_{twist} depends on tube radius cubically.[83] We use this fact and first-principles data[61] to estimate that k_{twist} values are 3021.2 eV/nm and 15809 eV/nm for armchair and zigzag CNTs of similar radii, respectively. Along similar lines, we also carried out axial stiffness calculations (further details in SI) while constraining the strain to ± 3.3%. In this range, the deformation energy displays a quadratic trend (Figure 1f), consistent with linear response. In particular, the extensional stiffness (k_{stretch}) for an armchair P_2C_3NT of radius 1.85 nm is about 2711.3 eV/nm and it is about 1257.4 eV/nm for a zigzag tube of radius 1.07 nm. To compare these numbers against k_{stretch} values of CNTs, we once again utilized scaling laws obtained from continuum theory and first-principles data.[61,83] We estimated that armchair and zigzag CNTs of similar radii as the P_2C_3NTs above, are expected to have k_{stretch} values equal to 13318.3 eV/nm and 7678.1 eV/nm for armchair and zigzag varieties, respectively. Overall, these stiffness calculations imply that P_2C_3NTs are significantly more compliant to torsional and axial strains, when compared to their conventional carbon counterparts. In turn, these findings imply lower values of (thickness normalized) Young's and shear moduli of P_2C_3 sheets, when compared to graphene.

The symmetry adapted first-principles calculations described above reveal that all pristine P_2C_3NTs are metallic. Remarkably, we observe that a P_2C_3NT with cyclic group order $\mathcal{N}$ (with $\mathcal{N} = n$ for zigzag (n, 0) and armchair (n, n) tubes), possesses $2\mathcal{N}$ nearly degenerate flat bands very close to the Fermi level (Figure 2). There is also an associated sharp peak in the electronic density of states (eDOS), suggesting the easy availability of electron-rich states in these tubes (see Figure 4 and Figure S8 in SI). These flat bands originate due to destructive interference of electron hopping within the Kagome-like structure formed by C and P atoms, specifically involving the p_z and p_{xy} orbitals. Since this is a geometric frustration effect, standard KS-DFT under the local density approximation (LDA) can adequately describe the electronic structure without needing on-site Coulomb correction, U. For

https://doi.org/10.1021/acs.jpclett.6c00091
J. Phys. Chem. Lett. XXXX, XXX, XXX−XXX

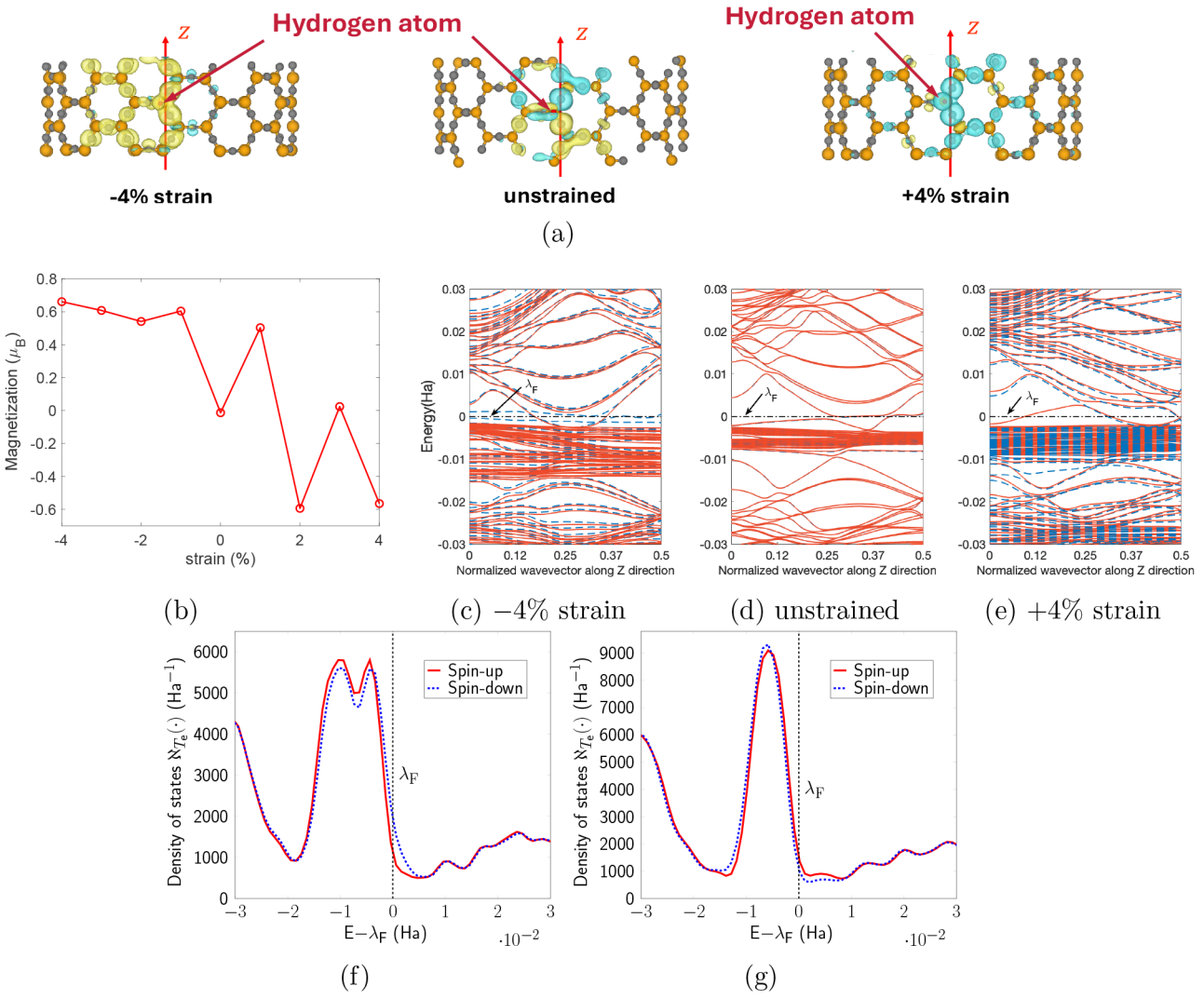

Figure 3. (a) Magnetization density isosurfaces for hydrogenated (9,9) armchair P_2C_3NT, where the hydrogen atom (red color) is attached to the phosphorus atom. The blue and yellow color clouds denotes the spin-down and spin-up electrons, respectively. (b) Evolution of the magnetization energy per unit cell with respect to the applied strain. (c),(d) and (e) show the band diagram for the −4% strain, unstrained and +4% strain cases, respectively. Spin-up and spin-down channels are represented by solid red and dashed blue lines, respectively. (f) and (g) show the spin DOS for 4% compression and tensile strain, respectively.

bands near the Fermi level, the flat band bandwidth (W) along the 1D Brillouin zone is approximately 35−78 meV for the armchair (9,9) nanotube, which is somewhat higher than the 13−22 meV observed for the zigzag (12,0) nanotube (electronic smearing for these calculations is 1 mHa, i.e., 27.2 meV). Plausible U values for p-orbitals in P and C atoms is typically $U \sim 1-3$ eV, making $U/W \gg 1$. Overall, these features are suggestive that P_2C_3NTs are likely to be a notable instance of quasi-one-dimensional materials that are inclined to display strongly correlated electronic states which are often associated with fascinating properties such as superconductivity and flat-band ferromagnetism.[84] Moreover, to our knowledge, the type of Dirac and flat-band coexistence at the Fermi level seen in P_2C_3NTs, has not been previously reported in a chemically realistic quasi-one-dimensional material.

As described above, in addition to the flat bands, the band structures of P_2C_3NTs also feature Dirac cones. In particular, for pristine armchair P_2C_3NTs, the flat band near the Fermi level (λ_F) touches a lower Dirac point near the gamma point ($\eta = 0$), and is separated from the upper Dirac point with a minute gap (~3.2 mHa for a (9,9) nanotube; Figure 2a). Two other sets of Dirac bands near $\eta = \pm 1/3$, which touch the flat band near λ_F , thereby making the tubes metallic, are also present. These crossings between the flat bands and Dirac points at $\eta = \pm 1/3$ are accidental rather than being symmetry-protected or the effect of curvature. Additionally, a family of quasi-flat bands reminiscent of the band structure of Kagome lattices with next-nearest neighbor interactions[35] are also present (in the energy range 35.2−70.4 mHa in Figure 2a). Similarly, zigzag P_2C_3NT also exhibit flat bands with Dirac points crossing near λ_F. However, kagome-like Dirac points which appear in the armchair nanotube are folded to the $\eta = 0$ point (labeled D_1 in Figure 2b) while rolling the sheet to form zigzag nanotubes. Overall, these arrangements of Dirac points at $\eta = \pm 1/3$ and $\eta = 0$ are reminiscent of the electronic structure of conventional armchair and zigzag CNTs, respectively.

https://doi.org/10.1021/acs.jpclett.6c00091
J. Phys. Chem. Lett. XXXX, XXX, XXX−XXX

To elucidate the orbital source and hybridization of the electronic band structure of the P_2C_3NTs studied here, we computed the projected density of states (pDOS). This allows us to estimate the contributions of the different orbitals of P and C atoms participating in the formation of energy bands near the Fermi level (Figure S1). From these calculations, it is evident that many of the electronic features of P_2C_3NTs largely originate from the participation of π electrons derived from radially oriented p_z (l = 1, m_l = 0) orbitals of both C and P atoms. Specifically, the flat bands arise from the individual π-electrons of C atoms, while the Dirac points situated at η = 0 near the Fermi level (in both armchair and zigzag tubes) are derived from the mixture of p_z orbitals of both P and C atoms (see Figure S1 (a) and (b)). Thus, the p_z orbitals in the nanotube create a bipartite honeycomb split graph lattice.[38] Indeed, the split graph operation applied to the bipartite honeycomb lattice introduces additional sites at the center of each edge, resulting in the lattice depicted in Figure 1a. This hybridization between p_z orbitals of P and C atoms lifts the degeneracy and separates the flat band from the Dirac cone at the Γ-point as shown in Figure 2a. On the other hand, in-plane p_{xy} orbitals of C atoms form a Kagome lattice resulting in Kagome-like bands. These groups of bands include the aforementioned quasi-flat bands in the 35.2−70.4 mHa range, and additional Dirac bands positioned near the Fermi level (at $\eta = \pm 1/3$ in armchair nanotubes and at η = 0 in zigzag nanotubes). These p_{xy} bands do not hybridize with the p_z flat band and form an accidental crossing at $\eta = \pm 1/3$ and 0 in armchair and zigzag nanotubes, respectively. Overall, the P_2C_3NTs bands are the direct sum of Honeycomb-Kagome bands and Kagome bands (also see Figure S1(c)).

The above analysis is also consistent with direct visualization of the spatial distribution of the wave functions (Figure 2c and 2d). Considering the band diagrams of two representative armchair and zigzag P_2C_3NTs (Figure 2a and 2b), we see that points P_2 and D_2 on the flat bands show the electrons localized to p_z-type atomic orbitals of C atoms(top right of Figures 2c, 2d). The lobes of these orbitals are pointing perpendicular to the θ_1 $-\theta_2$ plane, i.e., along the radial direction in the tube. In contrast, points P_3 and D_3 on the Dirac bands correspond to electronic states with in-plane p_{xy} orbital characteristics (bottom left of Figures 2c, 2d). Finally, points P_1 and D_1, which lie at the gamma point, are at the intersection of the Dirac cones and the flat bands, and are therefore associated with electronic states with both these characteristics. This is evident in the shapes of the corresponding orbitals (top left of Figures 2c, 2d).

Drawing insights from the pDOS calculations (see SI) and the discussion above, we constructed a next-nearest neighbor (NNN) symmetry-adapted tight binding (TB) model to capture the salient features of the electronic structure of P_2C_3NTs (see Figure S1). We utilized the Dresselhaus approach[78] and expressed the 8 bands-TB Hamiltonian in terms of two sets of orthogonal orbitals — three radially oriented p_z orbitals of C atoms, along with two more from P atoms and three in-plane p_{xy} orbitals C atoms. The results of our TB calculations for pristine P_2C_3NTs are illustrated in Figure S2(a) and (b). It is evident from these figures that there is a remarkable qualitative agreement between these results and the first-principles data presented earlier, thus lending support to our interpretation of the origin of the electronic features of P_2C_3NTs.

Flat bands with Coulomb interactions are often associated with magnetism.[84] However, in most flat-band materials, the electrons remain unpolarized. In the past, vacancies and hydrogenation of graphene and CNTs have been shown to induce magnetic order in these materials.[85−90] Taking cue from these studies, in Figure 3, we show that a (9,9) armchair P_2C_3NT can exhibit magnetic characteristics when a hydrogen atom is adsorbed by the phosphorus atom (one hydrogen atom per two periodic layers in axial direction considered). The presence of the hydrogen atom distorts the nanotube in the radial direction and induces anisotropy in the bond lengths and angles in the hexagonal plaquette. This breaks the local lattice symmetry and lifts the degeneracy of the flat bands in undeformed nanotube (Figure 3d), leading to nonzero magnetism. In the absence of external strain, the nanotube has contributions from both spin-up (yellow color isosurface) and spin-down (blue color isosurface) electrons, making the magnetic order ferrimagnetic-like with total magnetic moment of −0.0133 μ_B (middle column of Figure 3a). The spin-up and spin-down orbitals are largely localized on the carbon atoms closest to the hydrogen atom with the local magnetic moments being 0.109 μ_B and −0.116 μ_B.

Since structural distortion often plays an important role in tuning magnetism,[91,92] we next applied axial strain to the hydrogenated nanotube. Interestingly, under compressive strain the nanotube transitions from ferrimagnetic-like to ferromagnetic-like state, where most contribution to the magnetic order comes from the spin-up electrons (left panel of Figure 3a, corresponding to 4% compressive strain). The magnetization increases under compression and saturates to 0.66 μ_B at −4% strain. Under tensile strain, the nanotube exhibits a dynamic interplay between antiferromagnetic-like and ferromagnetic-like behaviors across different strain levels (see Figure 3b). In particular, the nanotube under +1% strain has majority spin-up states with 0.50 μ_B magnetization, after which the polarity switches to spin-down with −0.59 μ_B magnetization, at +2% strain. Upon further increasing the strain to +3% the nanotube becomes antiferromagnetic-like, and finally, under +4% strain it turns back to ferromagnetic-like order with magnetization −0.57 μ_B. Correspondingly, a high concentration of spin-down clouds is visible in the right column of Figure 3a. The strain induced ferromagnetic-like behavior can also be seen from the band diagrams and spin-DOS of two extreme strain cases, i.e., 4% compression (Figure 3c and 3f) and extension (Figure 3e and 3g), where the energy bands splits into spin-up (red solid lines) and spin-down (dashed blue lines) channels. Overall, this shows a remarkable example of controllable magnetic behavior in P_2C_3NTs where spin polarity can be changed with the application of strain.

To verify the robustness of the predicted magnetic states, additional spin-polarized calculations were performed using different initial magnetic moments on the H atom while keeping all other computational parameters unchanged. For both tensile and compressive strain, all calculations initialized with a finite magnetic moment converge to the same magnetic solution with a net magnetization magnitude of approximately 0.99 μB per periodic unit cell. Depending on the initial spin configuration, the final magnetization was found to appear with either positive or negative sign; however, these solutions correspond simply to globally spin-inverted states that are energetically equivalent within numerical precision, which is expected in collinear spin KS-DFT calculations. Calculations initialized with zero magnetic moment converge instead to a

https://doi.org/10.1021/acs.jpclett.6c00091
J. Phys. Chem. Lett. XXXX, XXX, XXX−XXX

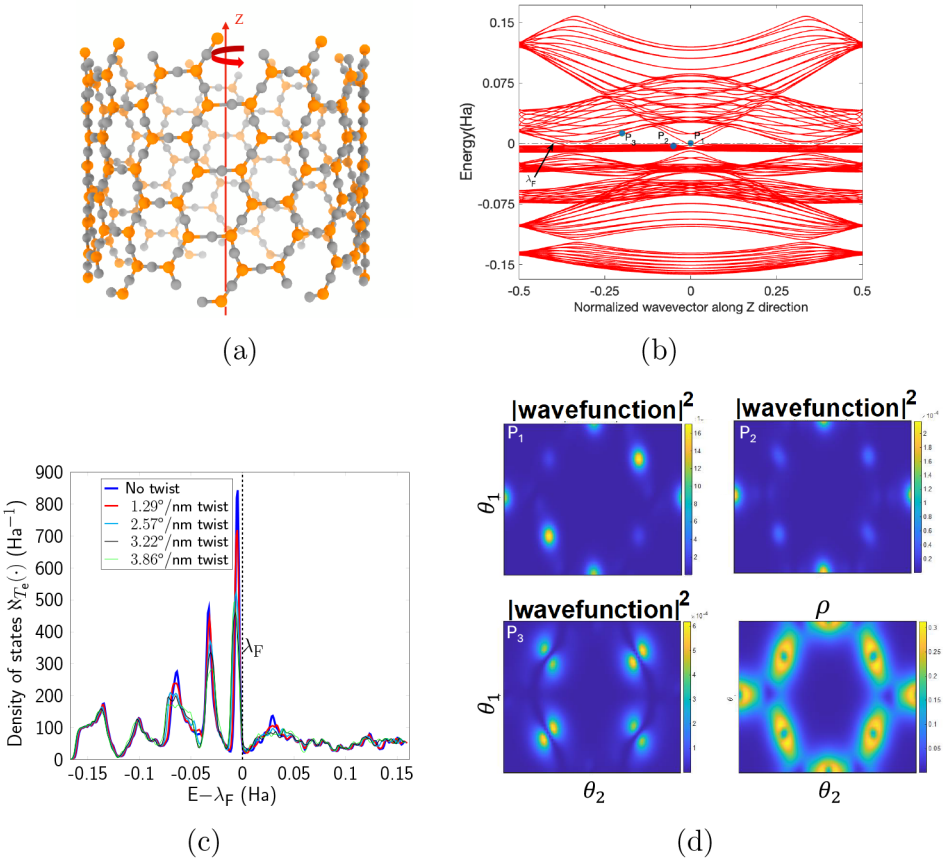

Figure 4. (a) Twisted armchair P_2C_3NT. (b) Band diagram of (9,9) twisted armchair P_2C_3NT at 3.86°/nm. The Fermi level λ_F corresponds to the x-axis. (c) Electronic density of states (eDOS) plot for different rate of twists. (d) shows the electronic states (square of absolute value of wave function) associated with the points P_1, P_2 and P_3 points shown in (b). Bottom right panel shows the electronic density ρ. A slice of electronic fields at an average radial distance of the atoms in the computational domain is shown. θ_1, θ_2 denote helical coordinates that parametrize the tube surface at a fixed radial distance.

nonmagnetic state that is slightly higher in energy than the spin-polarized solution. This indicates that the magnetic configuration represents the energetically favored ground state. Since the primitive periodic cell contains a single adsorption site, the present calculations probe the existence of a localized magnetic moment associated with hydrogen adsorption rather than a rigorously defined long-range magnetic ordering. The resulting spin polarization can therefore be interpreted as exhibiting ferromagnetic-like behavior within the unit cell. The relatively small energy difference between magnetic and nonmagnetic solutions suggests a soft, itinerant magnetic character, similar to defect-induced magnetism reported previously for hydrogenated carbon nanostructures.[92] The strain dependence of the magnetic moment arises from changes in the local electronic structure induced by deformation of the nanotube lattice. In particular, tensile or compressive strain modifies the P−H bond geometry and the hybridization between the hydrogen 1s orbital and neighboring phosphorus−carbon states, thereby altering the exchange splitting of the defect-derived electronic state responsible for the magnetic moment.

The above-discussed mechanism of generating unpaired spins without an external magnetic field may find applications in the emergent fields such as quantum hardware devices and spintronics. More realistic and detailed calculations of such magnetic effects (e.g., explicit inclusion of Hubbard corrections), especially within the context of device applications, form the scope of future work. A discussion of magnetism effects in P_2C_3NTs induced from a carbon vacancy is discussed in the SI. Notably, the periodically hydrogenated and vacancy configurations discussed here represent an idealized limit to maintain 1D translational periodicity. In realistic quasi-1D systems, random hydrogen adsorption or ionic vacancies may break translational symmetry and can induce disorder scattering.[93,94] Further studies of the effect of concentration of random disorder, dopant, torsional deformation and nanotube chirality on magnetic properties of P_2C_3NTs are all interesting subjects for future investigation.

Next, we investigated the general impact of applied strains to the electronic structure of P_2C_3NTs, and observed that both torsional and axial deformations disrupt the flat band degeneracy near the Fermi level. Increasing the applied strain leads to an increase in the energy width of the flat bands, accompanied by a decrease in flatness: for the maximum elastic strains considered here, the bandwidth of the flat bands near the Fermi level is 13.6−168.7 meV for the zigzag (12,0) tube under compression and 87.1−182.3 meV for the armchair (9,9) tube under twist. This is also demonstrated by the electronic density of states plots of twisted armchair and uniaxially compressed zigzag nanotubes shown in Figure 4c and Figure S9, respectively. The height of the sharp peak of the eDOS decreases with applied strain, and its width broadens near λ_F. Specifically, when torsional deformation is applied to the prototypical example of an armchair nanotube with group

https://doi.org/10.1021/acs.jpclett.6c00091
J. Phys. Chem. Lett. XXXX, XXX, XXX−XXX

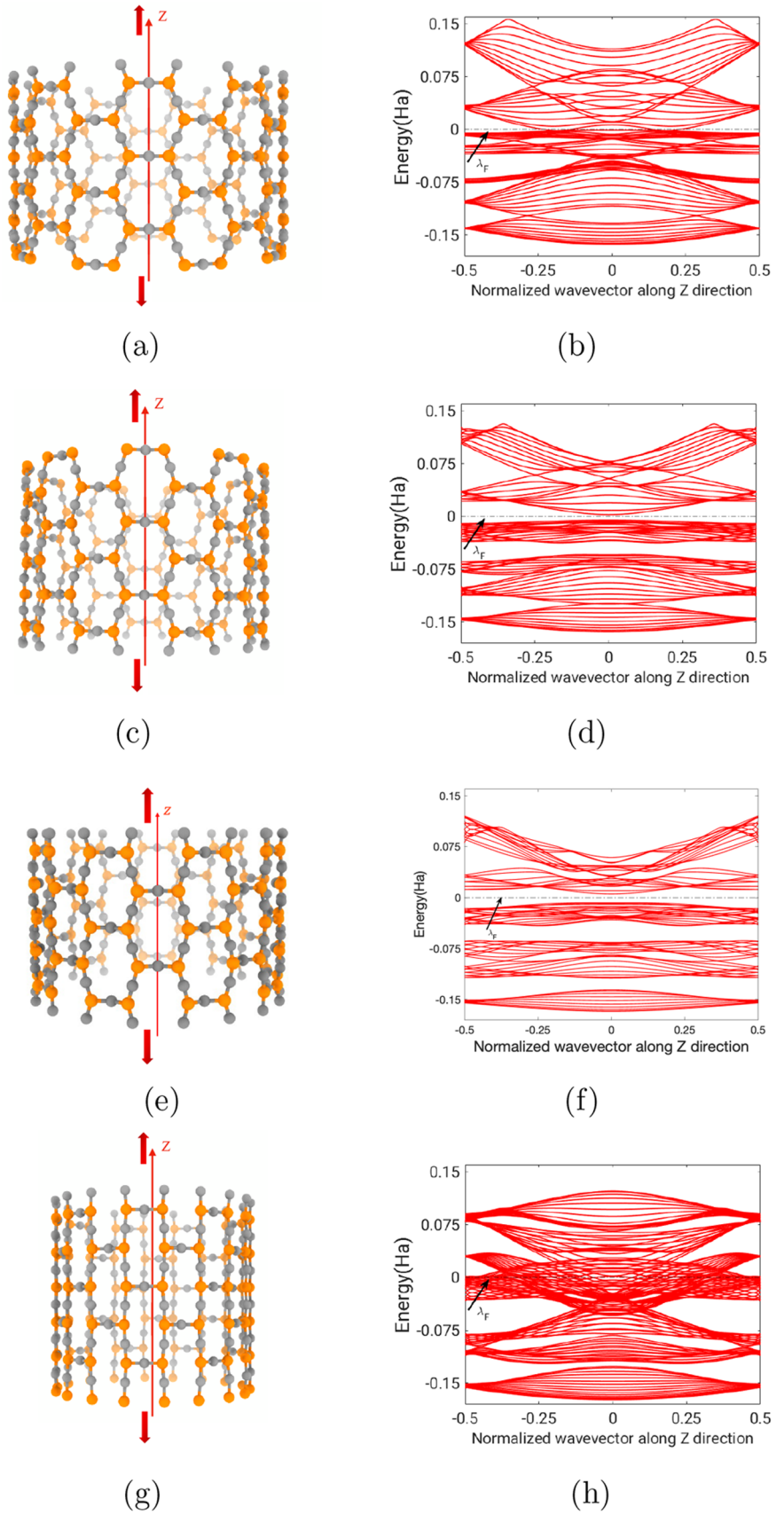

Figure 5. Structural and electronic phase transition of nanotube from pristine P_2C_3NT with hexagonal unit cell to the brick wall P_2C_3NT. Associated band diagrams are also shown. The arrows represent the direction of applied strain. (a) and (b) intermediate 6.35%, (c) and (d) intermediate 12.34%, (e) and (f) intermediate 18% and (g) and (h) brick wall 24.67%.

https://doi.org/10.1021/acs.jpclett.6c00091
J. Phys. Chem. Lett. XXXX, XXX, XXX−XXX

order $\mathcal{N} = 9$, the flat bands become slightly dispersive close to the $\eta = 0$ point, exhibiting partial flatness (Figure 4b). Although the gap diminishes between the top Dirac point and the flat bands, a minute gap emerges between the flat bands and the lower Dirac points situated at $\eta = 0$ and $\eta = \pm 1/3$. Interestingly, the electronic state corresponding to the point P_1 in armchair nanotube band diagrams (Figure 2c) has contribution from the p_z orbitals of both P and C atoms in an unstrained state, but it is concentrated only at the p_z atomic orbitals of carbon atoms under torsional strain (P_1 in Figure 4d). Simultaneously, the electronic state corresponding to point P_2 in the flat band is redistributed to other sets of carbon atoms (Figure 4d). However, the state corresponding to the point P_3 does not show a significant change in spatial distribution. Similarly, uniaxial strain also induces some degree of dispersion in the flat bands. As illustrated in the band structure of (12,0) zigzag nanotube under longitudinal compression of 3.28% (Figure S9(a)), the flat bands show comparatively no drastic changes near the $\eta = 0$ point. No significant effect of compression is observed on the spatial distribution of the electronic states either (see Figure S9(c)−(e)). The TB band structure for the twisted armchair nanotube and the uniaxially compressed zigzag nanotube is presented in Supporting Information (Figure S2(c) and (d)) agrees well with the ab inito results. Overall, the flat bands in both nanotubes exhibit some dispersion under small strains but remain largely robust, likely maintaining any strongly correlated electronic states in the material. This likely stems from the robustness of the electronic states in P_2C_3 sheets themselves to elastic strains (Figures S5, S6). Interestingly, this resilient behavior is in sharp contrast to other proposed 1D materials with flat bands (e.g., carbon Kagome nanotubes[32]), where small strains can break the local symmetries of the unit cell, thus introducing more noticeable dispersion into the flat bands. Usually, under such circumstances, the quadratic band touching point evolves into a pair of tilted Dirac cones.[32] This makes P_2C_3NTs a realistic quasi-one-dimensional material platform where stable and robust strongly correlated physics can be studied.

Continuing with our strain simulations, we next subjected the nanotubes to more extensive (inelastic) deformations, going up to the limit of failure. This leads to structural phase changes and triggers multiple quantum phase transitions. In particular, the armchair nanotube transforms into a "brick-wall"[95] structure due to large tensile strain exerted along the tube axis (Figure 5). This results in shrinking of the nanotube along the radial direction, which is reminiscent of the Poisson effect. To study the transformation pathways in the nanotubes, we first strained and optimized the underlying 2D lattices using a "freeze and relax" strategy[96] (details in the SI). Following this, we rolled up these structures to form nanotubes and carried out further structural relaxation to arrive at plausible low-energy transition states. Three transition points along the transformation pathway require special attention. At 6.35% strain, the triple degeneracy point at $\eta = 0$ is lifted and Dirac cones disappear (Figure 5b), thus signifying that this Dirac point is stable only for small deformation. Remarkably, however, some of the dispersion-less states are still intact near the Fermi level. On further increasing the strain to 12.34% the Dirac points of opposite vortices (Berry phase $\pm \pi$) at $\eta = \pm 1/3$ annihilate at the time-reversal invariant point ($\eta = 0$) and open a gap near the Fermi energy (see band diagram in Figure 5d), suggesting transition from the metallic state to the insulating phase. This phenomenon of annihilation of Dirac nodes due to high structural anisotropy has been previously investigated in NNN TB models of graphene[97] and Kagome lattices.[37,98−100] In the brick-wall structure at 24.67% strain, the bands become highly dispersive with multiple bands crossing the Fermi energy leading to another electronic phase transition from the insulating to the metallic state. This demonstrates that under large deformation P_2C_3NTs show fascinating electronic state transitions. Such structural and electronic transitions have been theoretically studied[95,101] in the literature, and have also been and experimentally explored in optical lattices.[102] P_2C_3NTs provide a realistic material platform to explore such phenomena further.

Recently, conventional CNTs have attracted attention from the perspective of 1D topological insulators, where the topology is characterized by the $\mathbb{Z}$ topological invariant (winding number).[103−107] The appearance of zero-energy edge states at the ends of finite-length CNTs of chirality (n, m) depends on the integer $\mathcal{N} = \gcd(n, m)$. Thus, only zigzag and chiral nanotubes with $\mathcal{N}$ not divisible by 3 show edge states, and armchair CNTs remain topologically trivial. Motivated by these considerations and the fact that P_2C_3NTs have an underlying hexagonal lattice, we performed symmetry adapted first-principles calculations and used (8,0) zigzag P_2C_3NTs as a prototypical example (both ends are zigzag-type). The edge states appearing at the valence band maximum (VBM) and the conduction band minimum (CBM) are shown in Figure 6a and 6b. The end states are toward the right-hand side for the VBM and the left-hand side for the CBM. Notably in the studies described above, we do not explicitly compute a winding number for P_2C_3NTs; our interpretation of the edge states is based on the CNT analogy, Berry-phase arguments, and the finite-length wave function localization. We expect that these edge states will appear in other chiral P_2C_3NTs, which invites further study. While it is well-known that Dirac points induce edge states due to nontrivial Berry phases,[108−110] in P_2C_3NTs the Dirac points intersect with the flat bands, thus suggesting both these electronic features are responsible for the edge states in this material. Our results show that P_2C_3NTs are

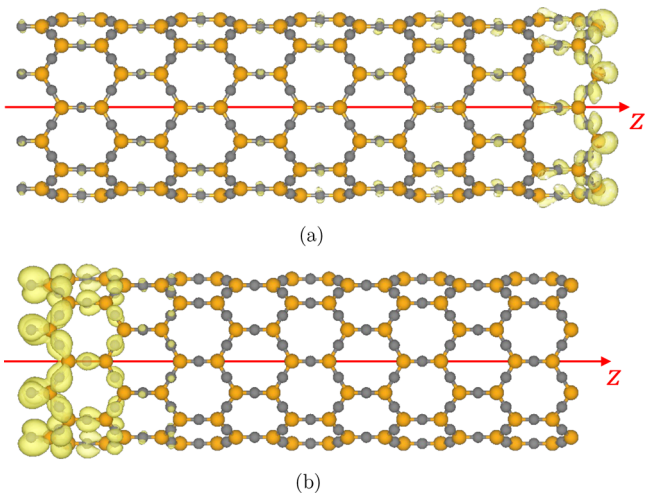

Figure 6. Isosurfaces of wave function (absolute value squared) of finite (8,0) zigzag P_2C_3NT at the (a) valence band maximum and (b) conduction band minimum. The wave function has higher concentration at the end of the nanotube.

https://doi.org/10.1021/acs.jpclett.6c00091
J. Phys. Chem. Lett. XXXX, XXX, XXX−XXX

an exciting example of a quasi-1D nanostructure that supports topological behavior and electron transport at the edges.

In summary, we have introduced P_2C_3NTs formed through a roll-up construction of monolayer phosphorus carbide (P_2C_3). Using symmetry adapted first-principles calculations and other theoretical tools, we extensively characterized two types of nanotubes, armchair and zigzag. These nanotubes provide an unique platform where both Dirac fermions and strongly correlated states coexist in a realistic 1D nanostructure. The orbital analysis shows that the electronic bands near the Fermi level are the direct sum of the band diagrams of honeycomb splitgraph and Kagome lattices. P_2C_3NTs develop magnetic order on creating a carbon vacancy or by doping with hydrogen, and the magnetic behavior is highly controllable via strain in the latter case. The flat band states in both types of nanotubes are robust to small deformation. Under large tensile strains, the nanotubes undergo a structural transition process to a "brick-wall" phase, and we observed various fascinating electronic phenomena including Dirac cone annihilation and multiple metal−insulator transitions in the transition pathway. The finite nanotube simulations show topological features in the form of the localized edge states induced by Dirac points and flat bands. Calculations of structural properties suggest that P_2C_3NTs are stable structures at the room temperature, and due to the relatively low bending energy of P_2C_3 sheets, may be easily fabricated. Many novel types of carbon and phosphorus allotrope have been successfully synthesized in recent years, and it seems likely that P_2C_3 nanotubes can be grown and investigated experimentally in the near future. Finally, further computational characterization, including explicit transport, many-body effects, finite temperature correlation calculations, as well as more reliable simulations of magnetic effects, form the scope of future work.

■ ASSOCIATED CONTENT

Supporting Information

The Supporting Information is available free of charge at https://pubs.acs.org/doi/10.1021/acs.jpclett.6c00091.

Discretization parameters for helical DFT, determination of deformation energies and torsional/extensional stiffness values, tight-binding model for P_2C_3NTs bands, band structures for some 2D P_2C_3 and some P_2C_3NTs, projected density of states, magnetism studies on carbon vacancy, and magnified band diagrams of some structures shown in main text (PDF)

■ AUTHOR INFORMATION

Corresponding Author

Amartya S. Banerjee − *Department of Materials Science and Engineering, University of California, Los Angeles, California 90095, United States;* orcid.org/0000-0001-5916-9167; Email: asbanerjee@ucla.edu

Authors

Shivam Sharma − *Department of Mechanical Science and Engineering, University of Illinois at Urbana−Champaign, Urbana, Illinois 61801, United States*

Chenhaoyue Wang − *Department of Materials Science and Engineering, University of California, Los Angeles, California 90095, United States*

Hsuan Ming Yu − *Department of Materials Science and Engineering, University of California, Los Angeles, California 90095, United States*

Complete contact information is available at: https://pubs.acs.org/10.1021/acs.jpclett.6c00091

Notes

The authors declare no competing financial interest.

■ ACKNOWLEDGMENTS

This work was primarily supported by grant DE-SC0023432 funded by the U.S. Department of Energy, Office of Science. This research used resources of the National Energy Research Scientific Computing Center, a DOE Office of Science User Facility supported by the Office of Science of the U.S. Department of Energy under Contract No. DE-AC02-05CH11231, using NERSC awards BES-ERCAP0033206, BES-ERCAP0025205, BES-ERCAP0025168, and BES-ERCAP0028072. A.S.B. acknowledges funding from UCLA's Council on Research (COR) Faculty Research Grant and the Faculty Career Development Award from UCLA. Contributions by S.S. to this manuscript were made mainly during his time at the University of Minnesota. S.S. would like to thank Richard D. James (University of Minnesota) for helpful discussions and for providing support through the Vannevar Bush Faculty Fellowship (Grant No. N00014-19-1-2623) and the Air Force Defense Research Sciences Program Grant No. FA9550-24-1-0344. The authors acknowledge the use of the GPT-5 (OpenAI) model to polish the language and edit grammatical errors in some sections of this manuscript. The authors subsequently inspected, validated and edited the text generated by the AI model, before incorporation. The authors also acknowledge help from Kartikey Srivastava (UCLA) for help with a few simulations during the preparation of a revised version of the manuscript.

■ REFERENCES

(1) Tokura, Y.; Kawasaki, M.; Nagaosa, N. Emergent functions of quantum materials. *Nat. Phys.* **2017**, *13*, 1056−1068.

(2) De Leon, N. P.; Itoh, K. M.; Kim, D.; Mehta, K. K.; Northup, T. E.; Paik, H.; Palmer, B.; Samarth, N.; Sangtawesin, S.; Steuerman, D. W. Materials challenges and opportunities for quantum computing hardware. *Science* **2021**, *372*, No. eabb2823.

(3) Giustino, F.; Lee, J. H.; Trier, F.; Bibes, M.; Winter, S. M.; Valentí, R.; Son, Y.-W.; Taillefer, L.; Heil, C.; Figueroa, A. I.; et al. The 2021 quantum materials roadmap. *Journal of Physics: Materials* **2020**, *3*, 042006.

(4) Basov, D.; Averitt, R.; Hsieh, D. Towards properties on demand in quantum materials. *Nature materials* **2017**, *16*, 1077−1088.

(5) Aiello, C. D.; Abendroth, J. M.; Abbas, M.; Afanasev, A.; Agarwal, S.; Banerjee, A. S.; Beratan, D. N.; Belling, J. N.; Berche, B.; Botana, A.; et al. A chirality-based quantum leap. *ACS Nano* **2022**, *16*, 4989−5035.

(6) Keimer, B.; Moore, J. The physics of quantum materials. *Nat. Phys.* **2017**, *13*, 1045−1055.

(7) Bauer, B.; Bravyi, S.; Motta, M.; Chan, G. K.-L. Quantum algorithms for quantum chemistry and quantum materials science. *Chem. Rev.* **2020**, *120*, 12685−12717.

(8) Ball, P. Quantum materials: Where many paths meet. *MRS Bull.* **2017**, *42*, 698−705.

(9) Mas-Balleste, R.; Gomez-Navarro, C.; Gomez-Herrero, J.; Zamora, F. 2D materials: to graphene and beyond. *Nanoscale* **2011**, *3*, 20−30.

(10) Novoselov, K. S.; Geim, A. K.; Morozov, S. V.; Jiang, D.; Katsnelson, M. I.; Grigorieva, I. V.; Dubonos, S.; et al. Firsov, Two-dimensional gas of massless Dirac fermions in graphene. *nature* **2005**, *438*, 197−200.
(11) Li, Z.; Zhuang, J.; Wang, L.; Feng, H.; Gao, Q.; Xu, X.; Hao, W.; Wang, X.; Zhang, C.; Wu, K.; et al. Realization of flat band with possible nontrivial topology in electronic Kagome lattice. *Science advances* **2018**, *4*, No. eaau4511.
(12) Castro Neto, A. H.; Guinea, F.; Peres, N. M. R.; Novoselov, K. S.; Geim, A. K. The electronic properties of graphene. *Reviews of modern physics* **2009**, *81*, 109.
(13) Peres, N. M. Colloquium Colloqium: The transport properties of graphene: An introduction. *Reviews of modern physics* **2010**, *82*, 2673.
(14) Falkovsky, L. A. Optical properties of graphene. *Journal of Physics: conference series* **2008**, *129*, 012004.
(15) Gomes, K. K.; Mar, W.; Ko, W.; Guinea, F.; Manoharan, H. C. Designer Dirac fermions and topological phases in molecular graphene. *Nature* **2012**, *483*, 306−310.
(16) Liu, C.-C.; Feng, W.; Yao, Y. Quantum spin Hall effect in silicene and two-dimensional germanium. *Physical review letters* **2011**, *107*, 076802.
(17) Derzhko, O.; Richter, J.; Maksymenko, M. Strongly correlated flat-band systems: The route from Heisenberg spins to Hubbard electrons. *International Journal of Modern Physics B* **2015**, *29*, 1530007.
(18) Balents, L.; Dean, C. R.; Efetov, D. K.; Young, A. F. Superconductivity and strong correlations in moiré flat bands. *Nat. Phys.* **2020**, *16*, 725−733.
(19) Iglovikov, V.; Hébert, F.; Grémaud, B.; Batrouni, G.; Scalettar, R. Superconducting transitions in flat-band systems. *Phys. Rev. B* **2014**, *90*, 094506.
(20) Peotta, S.; Törmä, P. Superfluidity in topologically nontrivial flat bands. *Nat. Commun.* **2015**, *6*, 8944.
(21) Pollmann, F.; Fulde, P.; Shtengel, K. Kinetic ferromagnetism on a kagome lattice. *Physical review letters* **2008**, *100*, 136404.
(22) Pons, R.; Mielke, A.; Stauber, T. Flat-band ferromagnetism in twisted bilayer graphene. *Phys. Rev. B* **2020**, *102*, 235101.
(23) Wu, C.; Bergman, D.; Balents, L.; Sarma, S. D. Flat bands and Wigner crystallization in the honeycomb optical lattice. *Physical review letters* **2007**, *99*, 070401.
(24) Tang, E.; Mei, J.-W.; Wen, X.-G. High-temperature fractional quantum Hall states. *Physical review letters* **2011**, *106*, 236802.
(25) Sun, K.; Gu, Z.; Katsura, H.; Sarma, S. D. Nearly flatbands with nontrivial topology. *Physical review letters* **2011**, *106*, 236803.
(26) Ortiz, B. R.; Sarte, P. M.; Kenney, E. M.; Graf, M. J.; Teicher, S. M.; Seshadri, R.; Wilson, S. D. Superconductivity in the Z 2 kagome metal KV 3 Sb 5. *Physical Review Materials* **2021**, *5*, 034801.
(27) Kim, S.-W.; Oh, H.; Moon, E.-G.; Kim, Y. Monolayer Kagome metals A V3Sb5. *Nat. Commun.* **2023**, *14*, 591.
(28) Wang, Y.; Wu, H.; McCandless, G. T.; Chan, J. Y.; Ali, M. N. Quantum states and intertwining phases in kagome materials. *Nature Reviews Physics* **2023**, *5*, 635−658.
(29) Ortiz, B. R.; Teicher, S. M.; Hu, Y.; Zuo, J. L.; Sarte, P. M.; Schueller, E. C.; Abeykoon, A. M.; Krogstad, M. J.; Rosenkranz, S.; Osborn, R.; et al. Cs V 3 Sb 5: AZ 2 topological kagome metal with a superconducting ground state. *Phys. Rev. Lett.* **2020**, *125*, 247002.
(30) Jiang, Y.-X.; Yin, J.-X.; Denner, M. M.; Shumiya, N.; Ortiz, B. R.; Xu, G.; Guguchia, Z.; He, J.; Hossain, M. S.; Liu, X.; et al. Unconventional chiral charge order in kagome superconductor KV3Sb5. *Nature materials* **2021**, *20*, 1353−1357.
(31) Tan, H.; Liu, Y.; Wang, Z.; Yan, B. Charge Density Waves and Electronic Properties of Superconducting Kagome Metals. *Phys. Rev. Lett.* **2021**, *127*, 046401.
(32) Yu, H. M.; Sharma, S.; Agarwal, S.; Liebman, O.; Banerjee, A. S. Carbon Kagome nanotubes—quasi-one-dimensional nanostructures with flat bands. *RSC Adv.* **2024**, *14*, 963−981.
(33) Du, L.; Zhou, X.; Fiete, G. A. Quadratic band touching points and flat bands in two-dimensional topological Floquet systems. *Phys. Rev. B* **2017**, *95*, 035136.
(34) Uebelacker, S.; Honerkamp, C. Instabilities of quadratic band crossing points. *Physical Review B Condensed Matter and Materials Physics* **2011**, *84*, 205122.
(35) Barreteau, C.; Ducastelle, F.; Mallah, T. A bird's eye view on the flat and conic band world of the honeycomb and Kagome lattices: towards an understanding of 2D metal-organic frameworks electronic structure. *J. Phys.: Condens. Matter* **2017**, *29*, 465302.
(36) Mizoguchi, T.; Kuno, Y.; Hatsugai, Y. Square-root higher-order topological insulator on a decorated honeycomb lattice. *Phys. Rev. A* **2020**, *102*, 033527.
(37) Jiang, W.; Kang, M.; Huang, H.; Xu, H.; Low, T.; Liu, F. Topological band evolution between Lieb and kagome lattices. *Phys. Rev. B* **2019**, *99*, 125131.
(38) Ma, D.-S.; Xu, Y.; Chiu, C. S.; Regnault, N.; Houck, A. A.; Song, Z.; Bernevig, B. A. Spin-orbit-induced topological flat bands in line and split graphs of bipartite lattices. *Physical review letters* **2020**, *125*, 266403.
(39) Mizoguchi, T.; Yoshida, T.; Hatsugai, Y. Square-root topological semimetals. *Phys. Rev. B* **2021**, *103*, 045136.
(40) Mellaerts, S.; Meng, R.; Menghini, M.; Afanasiev, V.; Seo, J. W.; Houssa, M.; Locquet, J.-P. Two dimensional V2O3 and its experimental feasibility as robust room-temperature magnetic Chern insulator. *npj 2D Materials and Applications* **2021**, *5*, 65.
(41) Hashmi, A.; Nakanishi, K.; Farooq, M. U.; Ono, T. Ising ferromagnetism and robust half-metallicity in two-dimensional honeycomb-kagome Cr2O3 layer. *npj 2D Materials and Applications* **2020**, *4*, 39.
(42) Zhang, S.-j.; Zhang, C.-w.; Zhang, S.-f.; Ji, W.-x.; Li, P.; Wang, P.-j.; Li, S.-s.; Yan, S.-s. Intrinsic Dirac half-metal and quantum anomalous Hall phase in a hexagonal metal-oxide lattice. *Phys. Rev. B* **2017**, *96*, 205433.
(43) Wang, H.; Yang, J.; Yu, Q.; Xiong, Y.; Huang, H.; Luo, S. First-principles Investigations on the Magnetic, Electronic, and Optical Properties of Honeycomb-Kagome-Structured Fe 2 O 3 Monolayer. *Journal of Superconductivity and Novel Magnetism* **2022**, *35*, 3353−3362.
(44) Wang, B.; Yuan, S.; Li, Y.; Shi, L.; Wang, J. A new Dirac cone material: a graphene-like Be 3 C 2 monolayer. *Nanoscale* **2017**, *9*, 5577−5582.
(45) Ji, W.-x.; Zhang, B.-m.; Zhang, S.-f.; Zhang, C.-w.; Ding, M.; Li, P.; Wang, P.-j. A planar C 3 Ca 2 film: a novel 2p Dirac half metal. *Journal of Materials Chemistry C* **2017**, *5*, 8504−8508.
(46) Pan, H.; Han, Y.; Li, J.; Zhang, H.; Du, Y.; Tang, N. Half-metallicity in a honeycomb−kagome-lattice Mg 3 C 2 monolayer with carrier doping. *Phys. Chem. Chem. Phys.* **2018**, *20*, 14166−14173.
(47) Liu, P.-F.; Bo, T.; Liu, Z.; Eriksson, O.; Wang, F.; Zhao, J.; Wang, B.-T. Hexagonal M2C3 (M= As, Sb, and Bi) monolayers: new functional materials with desirable band gaps and ultrahigh carrier mobility. *Journal of Materials Chemistry C* **2018**, *6*, 12689−12697.
(48) Huang, S.; Xie, Y.; Zhong, C.; Chen, Y. Double Kagome bands in a two-dimensional phosphorus carbide P2C3. *J. Phys. Chem. Lett.* **2018**, *9*, 2751−2756.
(49) Hu, Y.; Wang, J.; Lin, H. Metallic two-dimensional P2C3: a promising flexible anode for high-performance potassium-ion batteries. *Colloids Surf., A* **2021**, *619*, 126536.
(50) Li, M.; Wang, L.; Lei, H.; Yang, Y.; Li, Y.-Q.; Zhao, M.; Guan, J.; Li, W.; Qu, Y. Efficient helium and helium isotopes separation by phosphorus carbide P2C3 membrane. *Advanced Theory and Simulations* **2022**, *5*, 2100327.
(51) Guan, J.; Liu, D.; Zhu, Z.; Tománek, D. Two-dimensional phosphorus carbide: Competition between sp2 and sp3 bonding. *Nano Lett.* **2016**, *16*, 3247−3252.
(52) Kistanov, A. A.; Nikitenko, V. R.; Prezhdo, O. V. Point defects in two-dimensional γ-phosphorus carbide. *J. Phys. Chem. Lett.* **2021**, *12*, 620−626.
(53) Ma, X.; Zhou, J.; Yang, T.; Li, D.; Feng, Y. P. Phase diagram and superlattice structures of monolayer phosphorus carbide (P x C 1-x). *Physical Review Materials* **2021**, *5*, 024005.

https://doi.org/10.1021/acs.jpclett.6c00091
J. Phys. Chem. Lett. XXXX, XXX, XXX−XXX

(54) Chen, X.; Lin, J.; Lin, Q.; Li, R.; Xia, G.; Zou, W.; Yu, X. Two-dimensional CP 2 and Li x CP 2 (x= 1 and 2) monolayer with high-mobility transport anisotropy and extraordinary optical properties. *Phys. Rev. B* **2022**, *106*, 075402.
(55) Shcherbinin, S. A.; Zhou, K.; Dmitriev, S. V.; Korznikova, E. A.; Davletshin, A. R.; Kistanov, A. A. Two-dimensional black phosphorus carbide: Rippling and formation of nanotubes. *J. Phys. Chem. C* **2020**, *124*, 10235−10243.
(56) Kistanov, A.; Shcherbinin, S.; Huttula, M.; Cao, W. Starfish-like phosphorus carbide nanotubes. *Proceedings of the first virtual bilateral conference on funtional materials, BiC-FM*, October 8−9, 2020.
(57) Shcherbinin, S.; Ustiuzhanina, S.; Kistanov, A. Dynamical stability and electronic structure of β-phosphorus carbide nanowires. *Journal of Micromechanics and Molecular Physics* **2020**, *05*, 2050007.
(58) Dumitrica, T.; James, R. D. Objective molecular dynamics. *Journal of the Mechanics and Physics of Solids* **2007**, *55*, 2206−2236.
(59) Banerjee, A. S. Ab initio framework for systems with helical symmetry: theory, numerical implementation and applications to torsional deformations in nanostructures. *Journal of the Mechanics and Physics of Solids* **2021**, *154*, 104515.
(60) Banerjee, A. S.; Suryanarayana, P. Cyclic density functional theory: A route to the first principles simulation of bending in nanostructures. *Journal of the Mechanics and Physics of Solids* **2016**, *96*, 605−631.
(61) Yu, H. M.; Banerjee, A. S. Density functional theory method for twisted geometries with application to torsional deformations in group-IV nanotubes. *J. Comput. Phys.* **2022**, *456*, 111023.
(62) Ghosh, S.; Banerjee, A. S.; Suryanarayana, P. Symmetry-adapted real-space density functional theory for cylindrical geometries: Application to large group-IV nanotubes. *Phys. Rev. B* **2019**, *100*, 125143.
(63) Pathrudkar, S.; Yu, H. M.; Ghosh, S.; Banerjee, A. S. Machine learning based prediction of the electronic structure of quasi-one-dimensional materials under strain. *Phys. Rev. B* **2022**, *105*, 195141.
(64) Sharma, A.; Suryanarayana, P. Real-space density functional theory adapted to cyclic and helical symmetry: Application to torsional deformation of carbon nanotubes. *Phys. Rev. B* **2021**, *103*, 035101.
(65) Hohenberg, P.; Kohn, W. Inhomogeneous electron gas. *Physical review* **1964**, *136*, B864.
(66) Kohn, W.; Sham, L. J. Self-consistent equations including exchange and correlation effects. *Physical review* **1965**, *140*, A1133.
(67) Perdew, J. P.; Wang, Y. Accurate and simple analytic representation of the electron-gas correlation energy. *Phys. Rev. B* **1992**, *45*, 13244.
(68) Troullier, N.; Martins, J. L. Efficient pseudopotentials for plane-wave calculations. *Phys. Rev. B* **1991**, *43*, 1993.
(69) Hamann, D. Optimized norm-conserving Vanderbilt pseudopotentials. *Physical Review B Condensed Matter and Materials Physics* **2013**, *88*, 085117.
(70) Banerjee, A. S.; Suryanarayana, P.; Pask, J. E. Periodic Pulay method for robust and efficient convergence acceleration of self-consistent field iterations. *Chem. Phys. Lett.* **2016**, *647*, 31−35.
(71) Giannozzi, P.; Baroni, S.; Bonini, N.; Calandra, M.; Car, R.; Cavazzoni, C.; Ceresoli, D.; Chiarotti, G. L.; Cococcioni, M.; Dabo, I.; et al. QUANTUM ESPRESSO: a modular and open-source software project for quantum simulations of materials. *J. Phys.: Condens. Matter* **2009**, *21*, 395502.
(72) Giannozzi, P.; Baseggio, O.; Bonfà, P.; Brunato, D.; Car, R.; Carnimeo, I.; Cavazzoni, C.; De Gironcoli, S.; Delugas, P.; Ferrari Ruffino, F. Quantum ESPRESSO toward the exascale. *J. Chem. Phys.* **2020**, *152*, 154105.
(73) Xu, Q.; Sharma, A.; Comer, B.; Huang, H.; Chow, E.; Medford, A. J.; Pask, J. E.; Suryanarayana, P. SPARC: Simulation package for ab-initio real-space calculations. *SoftwareX* **2021**, *15*, 100709.
(74) Ghosh, S.; Suryanarayana, P. SPARC: Accurate and efficient finite-difference formulation and parallel implementation of Density Functional Theory: Extended systems. *Comput. Phys. Commun.* **2017**, *216*, 109−125.
(75) Ghosh, S.; Suryanarayana, P. SPARC: Accurate and efficient finite-difference formulation and parallel implementation of density functional theory: Isolated clusters. *Comput. Phys. Commun.* **2017**, *212*, 189−204.
(76) Cai, K.; Wan, J.; Wei, N.; Cai, H.; Qin, Q.-H. Thermal stability of a free nanotube from single-layer black phosphorus. *Nanotechnology* **2016**, *27*, 235703.
(77) Guan, L.; Chen, G.; Tao, J. Prediction of the electronic structure of single-walled black phosphorus nanotubes. *Phys. Chem. Chem. Phys.* **2016**, *18*, 15177−15181.
(78) Dresselhaus, M. S.; Dresselhaus, G.; Eklund, P.; Rao, A. *Carbon nanotubes*; Springer: 2000.
(79) Zhang, H.; Yao, Z.; Wang, J.; Zhong, W. Phonon dispersion analysis of carbon nanotubes based on inter-belt model and symplectic solution method. *International Journal of Solids and Structures* **2007**, *44*, 6428−6449.
(80) Saito, R.; Takeya, T.; Kimura, T.; Dresselhaus, G.; Dresselhaus, M. Raman intensity of single-wall carbon nanotubes. *Phys. Rev. B* **1998**, *57*, 4145.
(81) Jishi, R.; Venkataraman, L.; Dresselhaus, M.; Dresselhaus, G. Phonon modes in carbon nanotubules. *Chem. Phys. Lett.* **1993**, *209*, 77−82.
(82) Schmidt, O. G.; Eberl, K. Thin solid films roll up into nanotubes. *Nature* **2001**, *410*, 168−168.
(83) Timoshenko, S.; Young, D. H. *Elements of strength of materials*; Van Nostrand: 1968.
(84) Chen, Y.; Xu, S.; Xie, Y.; Zhong, C.; Wu, C.; Zhang, S. Ferromagnetism and Wigner crystallization in kagome graphene and related structures. *Phys. Rev. B* **2018**, *98*, 035135.
(85) Bhatt, M. D.; Kim, H.; Kim, G. Various defects in graphene: a review. *RSC Adv.* **2022**, *12*, 21520−21547.
(86) Banhart, F.; Kotakoski, J.; Krasheninnikov, A. V. Structural defects in graphene. *ACS Nano* **2011**, *5*, 26−41.
(87) Ma, Y.; Lehtinen, P.; Foster, A. S.; Nieminen, R. M. Magnetic properties of vacancies in graphene and single-walled carbon nanotubes. *New J. Phys.* **2004**, *6*, 68.
(88) Yazyev, O. V. Magnetism in disordered graphene and irradiated graphite. *Physical review letters* **2008**, *101*, 037203.
(89) Park, N.; Yoon, M.; Berber, S.; Ihm, J.; Osawa, E.; Tománek, D. Magnetism in all-carbon nanostructures with negative Gaussian curvature. *Physical review letters* **2003**, *91*, 237204.
(90) Yang, X.; Dong, J. Ferromagnetism of an all-carbon composite composed of a carbon nanowire inside a single-walled carbon nanotube. *Appl. Phys. Lett.* **2005**, *86*, 163105.
(91) Boukhvalov, D.; Katsnelson, M.; Lichtenstein, A. Hydrogen on graphene: Electronic structure, total energy, structural distortions and magnetism from first-principles calculations. *Physical Review B Condensed Matter and Materials Physics* **2008**, *77*, 035427.
(92) Yang, X.; Wu, G. Itinerant flat-band magnetism in hydrogenated carbon nanotubes. *ACS Nano* **2009**, *3*, 1646−1650.
(93) Ostrovsky, P.; Gornyi, I.; Mirlin, A. Electron transport in disordered graphene. *Physical Review B Condensed Matter and Materials Physics* **2006**, *74*, 235443.
(94) Yuan, S.; Roldán, R.; De Raedt, H.; Katsnelson, M. I. Optical conductivity of disordered graphene beyond the Dirac cone approximation. *Phys. Rev. B* **2011**, *84*, 195418.
(95) Hou, J.-M.; Chen, W. Hidden symmetry and protection of Dirac points on the honeycomb lattice. *Sci. Rep.* **2015**, *5*, 17571.
(96) Suwannakham, P.; Sagarik, K. Dynamics of structural diffusion in phosphoric acid hydrogen-bond clusters. *RSC Adv.* **2017**, *7*, 21492−21506.
(97) Bernevig, B. A. *Topological insulators and topological superconductors*; Princeton University Press: 2013.
(98) Lim, L.-K.; Fuchs, J.-N.; Piéchon, F.; Montambaux, G. Dirac points emerging from flat bands in Lieb-kagome lattices. *Phys. Rev. B* **2020**, *101*, 045131.
(99) Montambaux, G.; Lim, L.-K.; Fuchs, J.-N.; Piéchon, F. Winding vector: how to annihilate two Dirac points with the same charge. *Physical review letters* **2018**, *121*, 256402.

https://doi.org/10.1021/acs.jpclett.6c00091
J. Phys. Chem. Lett. XXXX, XXX, XXX−XXX

(100) Montambaux, G.; Piéchon, F.; Fuchs, J.-N.; Goerbig, M. O. Merging of Dirac points in a two-dimensional crystal. *Phys. Rev. B* **2009**, *80*, 153412.
(101) Hou, J.-M. Hidden-symmetry-protected topological semimetals on a square lattice. *Phys. Rev. Lett.* **2013**, *111*, 130403.
(102) Tarruell, L.; Greif, D.; Uehlinger, T.; Jotzu, G.; Esslinger, T. Creating, moving and merging Dirac points with a Fermi gas in a tunable honeycomb lattice. *Nature* **2012**, *483*, 302−305.
(103) Okuyama, R.; Izumida, W.; Eto, M. Topological classification of the single-wall carbon nanotube. *Phys. Rev. B* **2019**, *99*, 115409.
(104) Izumida, W.; Okuyama, R.; Yamakage, A.; Saito, R. Angular momentum and topology in semiconducting single-wall carbon nanotubes. *Phys. Rev. B* **2016**, *93*, 195442.
(105) Okuyama, R.; Izumida, W.; Eto, M. Topological phase transition in metallic single-wall carbon nanotube. *J. Phys. Soc. Jpn.* **2017**, *86*, 013702.
(106) Moca, C. P.; Izumida, W.; Dóra, B.; Legeza, Ö.; Asbóth, J. K.; Zaránd, G. Topologically protected correlated end spin formation in carbon nanotubes. *Phys. Rev. Lett.* **2020**, *125*, 056401.
(107) Izumida, W.; Milz, L.; Marganska, M.; Grifoni, M. Topology and zero energy edge states in carbon nanotubes with superconducting pairing. *Phys. Rev. B* **2017**, *96*, 125414.
(108) Wakabayashi, K.; Takane, Y.; Yamamoto, M.; Sigrist, M. Electronic transport properties of graphene nanoribbons. *New J. Phys.* **2009**, *11*, 095016.
(109) Ando, T. Theory of electronic states and transport in carbon nanotubes. *J. Phys. Soc. Jpn.* **2005**, *74*, 777−817.
(110) Ryu, S.; Hatsugai, Y. Topological origin of zero-energy edge states in particle-hole symmetric systems. *Physical review letters* **2002**, *89*, 077002.

https://doi.org/10.1021/acs.jpclett.6c00091
J. Phys. Chem. Lett. XXXX, XXX, XXX−XXX